Chapter 12

Models for Metal/Ceramic Interface Fracture

ZHIGANG SUO
C. FONG SHIH

Metal-matrix composites are excellent candidate materials for advanced engineering systems. However, they have one major shortcoming that has limited their widespread use—their tendency to fracture easily. In many systems, the low ductility or brittleness of these composites is caused by microfailure processes that invariably begin at the interfaces. Thus, the mechanical behavior and the overall performance of metal-matrix composites are not limited by bulk properties or bulk phases, but by interface properties and toughness. Theories on interface fracture are reviewed in this chapter. With few exceptions, attention is limited to continuum mechanics considerations. Readers are referred to Rice et al. (1989, 1990, 1992) and references therein for atomistic and thermodynamic aspects of this subject. This article is concerned with recent advances within the confines of small-scale inelasticity and loading conditions, such that a major portion of the crack faces remain open. We review works regarding relatively brittle interfaces where the inelastic zone is small compared to the overall component. Large-scale bridging is reviewed by Bao and Suo (1992). Large scale contact has been treated by Hutchinson and Jensen (1990) within the context of fiber pullout against frictional sliding. The focus of this article is on theories. For a broader coverage of topics, the reader is referred to published proceedings of symposia on interfacial fracture. These include those edited by Suresh and Needleman (1989), Rühle et al. (1990), and Ashby et al. (1992). Experimental aspects of interface fracture and fatigue are reviewed by Evans et al. (1990), Kim (1991), and Cannon et al. (1992). Several aspects of fatigue are also discussed in a recent article (Woeltjen et al. 1992).

The mechanics of interface fracture has its root in the earlier works of Griffith (1921) and Irwin (1960) on the general theory of fracture, of Williams (1959) on the elastic stress distribution around an interface crack, of England (1965), Erdogan (1965), and Rice and Sih (1965) on explicit solutions for interface cracks, and of many practicing engineers on ingenious methods to measure adhesive strength of bonds. However, the subject did not take off until the 1980s. Advanced composites for high temperature engines, and layered materials for microelectronic and optical devices, have been the main technical driving force for new theoretic developments. Rapid advancement in high-resolution microscopes, high-speed computers, and the general theory of fracture have all provided tools for solving these challenging technical problems.

The classical fracture mechanics, as advanced by Irwin (1960), Rice (1968), and Hutchinson (1979), and as summarized in the textbook by Kanninen and Popelar (1985), is largely phenomenological. It enables us to predict, without a detailed description of the crack tip processes, crack growth in a structure by utilizing the observed crack growth behavior in a fracture specimen. This approach relies on the existence of stress intensity factor and on fracture resistance measured by mechanical testing. The advantage and the deficiency of this black-box approach both originate from the same fact: this approach requires little, nor does it generate much, knowledge of the physical process of fracture.

Mechanism-based fracture mechanics attempts to link the fracture resistance to the microstructural variables, providing guidelines for processing better and newer materials. This approach is as old, if not as fully developed, as the phenomenological approach. Indeed, in his original paper, Griffith prescribed a phenomenological fracture criterion as well as a physical mechanism of fracture resistance: rearranging atoms in a bulk into surfaces requires energy. It was eminently clear to Irwin that any form of heat dissipation that accompanies fracture, such as plastic flow in metals, contributes to fracture resistance. But just how atomic separation and irreversible atomic movements are interconnected remains an open question even today. Partial theories, each valid for a particular mechanism at a particular length scale, have been devised, largely in the earlier works by Cottrell (1963) and Rice and Johnson (1970) on hole growth, by Ritchie et al. (1973) on cleavage of alloys, and by Aveston et al. (1971) on fiber reinforced components. An example of the success of the mechanism-based approach is the thorough understanding of advanced ceramics toughened by ductile particles, or transforming particles, or strong fibers that has been achieved (Evans 1990). As a by-product of the mechanism-based approach, short cracks, small components, and nagging questions in the framework of classical fracture mechanics can be addressed with a unified, conceptually simple viewpoint (Stump and Budiansky 1989; Bao and Suo 1992). The dual approach, phenomenological and mechanism-based, is kept in mind throughout this review article.

The chapter is organized as follows. Section 12.1 reviews the energy consideration for a traction-free interface crack under small-scale inelasticity conditions, leading to the concepts of debond driving force, $\mathcal{G}$, and debond resistance, Γ. Supplemented by elasticity solutions of $\mathcal{G}$ for given components and loading conditions and experimentally measured Γ for given materials, this energy consideration is sufficient for most engineering applications. Section 12.2 reviews Williams' solution for an interface crack between two elastic half spaces. The near-tip stress field lends itself to a precise definition of mode mixity; the near-tip opening sets the condition for small-scale contact. Calibration of fracture specimen is also discussed. Crack-tip plasticity is reviewed in Section 12.3. The relevant mode mixity is the ratio of shear over tension on the interface immediately outside of the plastic zone. The plastic zone size is shown to depend on the mode mixity, as is the opening of the blunted crack tip. An analysis of a metal foil sandwiched between two ceramic plates is included, demonstrating the effect of constrained plastic flow on the fracture resistance. Section 12.4 reviews results on growing cracks and the concepts leading to a fundamental understanding of fracture resistance. Included are crack growth in elastic-plastic materials, crack bridging with or without background plasticity, and cleavage in the presence of plastic flow.

12.1 Energy Balance

The following energy arguments are essentially the same as those of Griffith (1921) and Irwin (1960). Cracks often run when a test-piece is still predominantly elastic, inelastic deformation being localized in thin layers beneath the crack surfaces. Taking advantage of this fact, one can partition the total energy supplied by the applied work into (1) elastic energy stored in the test-piece and (2) the heat dissipated by plastic flow and residual energy stored in the thin layers. From (1) comes a definition of debond driving force, $\mathcal{G}$, and from (2) comes debond resistance, Γ. Obviously, this partition becomes meaningless when the inelastic deformation spreads over a large part of the test-piece, either because the test-piece is small, or because the material is very ductile. These have been reviewed elsewhere (Stump and Budiansky 1989; Bao and Suo 1992).

12.1.1 Debond Driving Force

Consider an interface crack extending over an area A (Figure 12.1). Material near the crack front undergoes inelastic deformation; the interface is usually ill defined, containing misfit dislocations, an interdiffusion zone, or reaction compounds. However, these zones are typically small compared to the overall dimension of the test-piece, so that the crack front can be treated as a mathematical line, and the interface a mathematical plane. In computing the elastic energy stored in the test-piece, the two solids are taken to be (possibly nonlinearly) elastic. That is, each solid can be described by a strain energy density function $w(\epsilon_{11}, \epsilon_{12}, ...)$, such that stresses σ_{ij} are derived from

$$dw = \sigma_{ij} d\epsilon_{ij} \tag{12.1}$$

Coupled with equilibrium and compatibility equations, these considerations define an elasticity problem. In particular, stress and strain are computed everywhere in the test-piece, down to the crack front and the interface; likewise the energy density w is computed everywhere. The elastic energy stored in the test-piece is an integral extended over the entire test-piece, such that

$$U = \int_V w dV \tag{12.2}$$

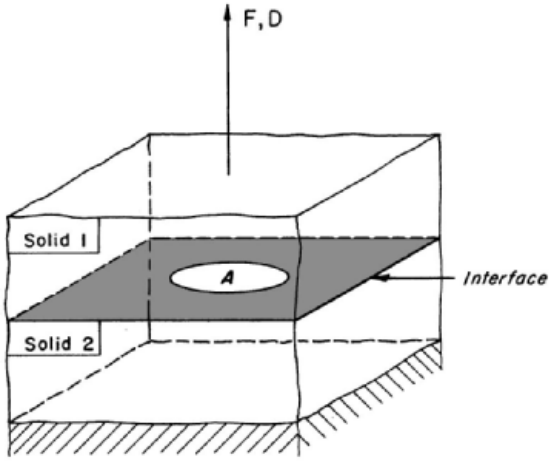

Figure 12.1. A partially debonded interface is subjected to applied load.

The test-piece in Figure 12.1 is loaded by displacement D, with work-conjugating force F. The elastic energy U depends on applied displacement and the crack size, thus,

$$U = U(D,A) \tag{12.3}$$

Note that U also depends on the geometry of the test-piece and the elastic moduli, but they remain constant during testing.

Upon loading, U varies as

$$dU = FdD - \mathcal{G}dA \tag{12.4}$$

With crack size held fixed ($dA = 0$), the above equation simply states that the energy increment equals the work applied. Because all the other quantities are defined, Equation 12.4 defines the quantity $\mathcal{G}$ when $dA \neq 0$. Just as F is the driving force for D, $\mathcal{G}$ is the driving force for crack size A. Explicitly, $\mathcal{G}$ is the decrease of elastic energy associated with a unit increment of crack area:

$$\mathcal{G} = -\frac{\partial U(D,A)}{\partial A} \tag{12.5}$$

Note that $\mathcal{G}$ has dimension energy/area.

The above concepts can be explained graphically. Figure 12.2(a) shows a load-displacement curve of the test-piece measured with fixed crack size ($dA = 0$). The curve should be straight for linear elastic materials. From Equation 12.4, U is the area under the load-displacement curve. Figure 12.2(b) shows two such load-displacement curves, measured in two independent tests with slightly different crack sizes, A and $A + dA$. The test-piece with the larger crack is more compliant; the shaded area is the energy decrease, dU, associated with dA. In early days, this graphical interpretation was employed to experimentally determine $\mathcal{G}$ (Rivlin and Thomas 1953).

Standard thermodynamics manipulations apply to the present discussions. For load-controlled tests, for example, it is more convenient to work with the potential energy

$$\Pi = U - FD \tag{12.6}$$

which is indicated in Figure 12.2(a). The independent variables are now F and A. Upon loading, Equation 12.4 becomes

$$d\Pi = -DdF - \mathcal{G}dA \tag{12.7}$$

Therefore, an alternative definition of $\mathcal{G}$ is

$$\mathcal{G} = -\frac{\partial \Pi(F,A)}{\partial A} \tag{12.8}$$

The definitions (12.5) and (12.8) are of course equivalent.

For an interface along the x_1-axis, and with displacement and traction continuous across the interface, Rice's J-integral (1968)

$$J = \int (wn_1 - n_i\sigma_{ij}u_{j,1})\, ds \tag{12.9}$$

vanishes over contours not enclosing any singularity. For a traction-free crack on the interface, $\mathcal{G}$ equals the J-integral over any path that begins at a point on the

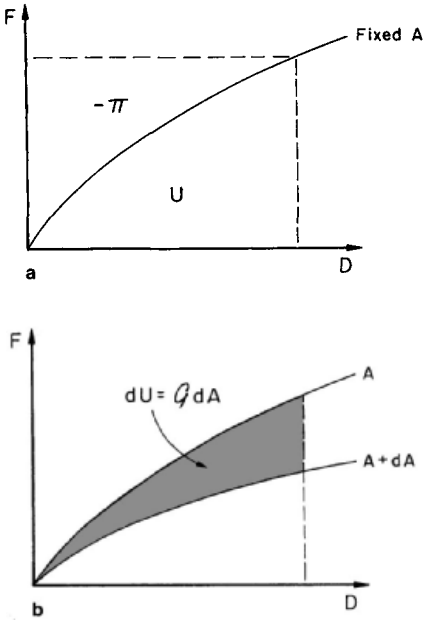

Figure 12.2. Graphic interpretation of (a) U and π and (b) $\mathcal{G}$.

lower crack face, and ends at another point on the upper crack face. This provides a tool for calculating $\mathcal{G}$ in finite element analysis (Moran and Shih 1987).

In general, $\mathcal{G}$ can be computed with an elasticity analysis of a given test-piece. Several illustrations requiring only elementary mechanics are given. Solutions to a wide range of geometries can be found in Hutchinson and Suo (1992) and the references therein.

Consider a fiber being pulled out of a matrix (Figure 12. 3). The energy stored in the fiber can be estimated by regarding the fiber as a tensile bar, clamped at the debond front. The pullout displacement is $D = L\sigma/E$, so that $U = (\sigma^2/2E)(\pi R^2 L)$. The potential energy is

$$\Pi(\sigma,L) = -\frac{\sigma^2}{2E}\pi R^2 L. \qquad (12.10)$$

Because the debond area is $A = 2\pi RL$, carrying out the differentiation in Equation 12.8 gives

$$\mathcal{G} = R\sigma^2/4E \qquad (12.11)$$

The estimate, which ignores the compliance of the fiber-matrix junction, is accurate when the debond length is large compared to the fiber diameter. Observe that $\mathcal{G}$ does not depend on the debond length L. Once debond starts, it will run to the other end of the fiber without any increase in load.

Thin-film cracking of many patterns has inspired a new problem area (Evans et al. 1988; Hutchinson and Suo 1992). Figure 12.4 illustrates a circular interface crack emanating from the edge of a hole in a thin film, driven by a residual tensile stress in the film. The stress in the debonded film is partially relieved, leading to a reduction in the elastic strain energy. The debonded film may be treated as a ring in plane stress, clamped at the debond front. The energy release rate is found to be

$$\mathcal{G} = \frac{2hE\varepsilon_0^2}{1-\nu^2}\left[1 + \frac{1-\nu}{1+\nu}\left(\frac{a}{a_0}\right)^2\right]^{-2} \qquad (12.12)$$

where ε_0 is the mismatch strain between the film and the substrate caused by thermal or epitaxial mismatch,

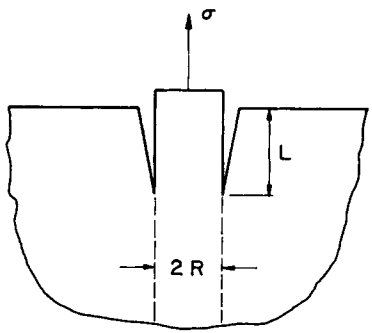

Figure 12.3. A fiber is being pulled out from a matrix.

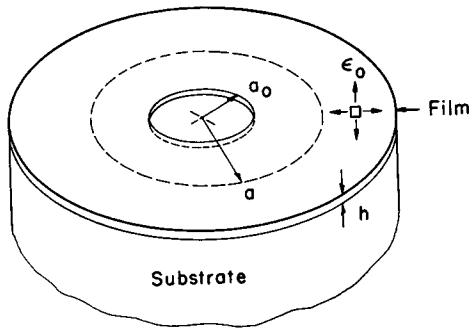

Figure 12.4. Thin-film decohesion emanating from a circular hole.

a_0 is the hole radius, a is the debond radius, and E and ν are the elastic constants of the film (Farris and Bauer 1988). Observe that $\mathcal{G}$ decreases rapidly as a increases, so that the debond is stable. Also note that $\mathcal{G}$ scales linearly with film thickness h: the thinner the film, the smaller the decohesion area. Debond can be practically suppressed if the film is sufficiently thin.

12.1.2 Debond Resistance

The essential idea of Griffith and Irwin is illustrated in Figure 12.5. Inelastic processes, such as atomic separation, twinning, phase transformation, and dislocation motion, require sufficiently high stress to activate, so they are confined to a region close to the crack tip where the stress is intensified. As the crack front extends, thin layers beneath the crack surface are left in the wake in which the atoms have undergone irreversible movements. The processes near the tip are complex and the quantification requires detailed knowledge of deformation mechanisms. Nonetheless, an effectively uniform deformation state along the x_1-axis is attained in the wake. Consider two cylinders of unit cross-sectional area normal to the interface, one far ahead of the crack front (A), and the other far behind (B). Let Γ be the energy spent to transform cylinder A to cylinder B. Obviously Γ depends on the deformation history that cylinder B underwent, including surface energy, heat dissipation, and elastic energy trapped in the wake.

The total energy variation, elastic as well as inelastic, is given by

$$FdD - \mathcal{G}dA + \Gamma dA \qquad (12.13)$$

When D is held fixed, no work is externally applied to the test-piece and the total energy remains unchanged, so that

$$\mathcal{G} = \Gamma \qquad (12.14)$$

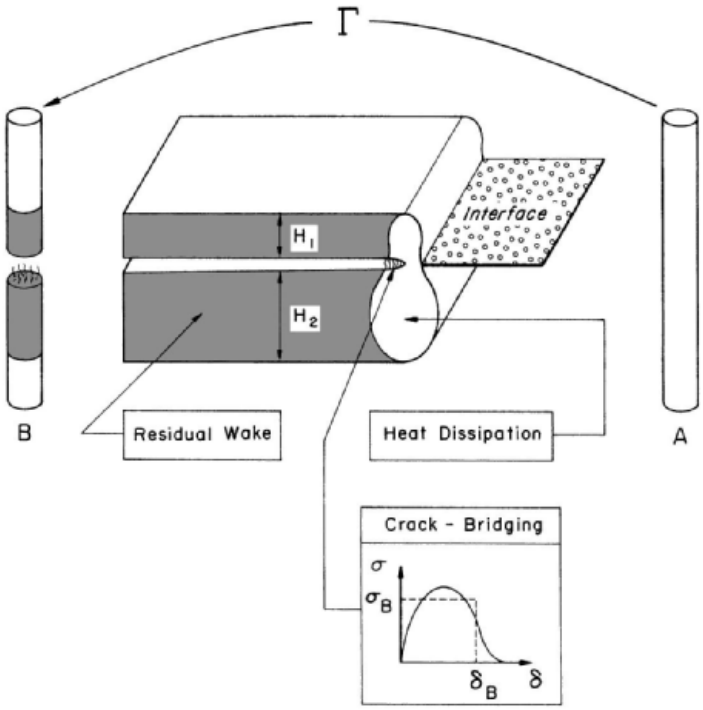

Figure 12.5. Inelastic processes accompanying debond.

The driving force $\mathcal{G}$ depends on the test-piece and can be evaluated by an elastic stress analysis. Fracture resistance Γ depends on the inelastic mechanisms. Equation 12.14 provides a connection between the macroscopic loading condition of a test-piece and the microscopic inelastic process associated with debonding.

Debond resistance can be measured phenomenologically. For example, this can be carried out using the fiber pullout experiment shown in Figure 12.3. The stress required to drive debond is measured, which can be translated to Γ using Equation 12.11 and noting Equation 12.14. This approach is purely phenomenological—no detailed knowledge of physical processes is required, nor is such knowledge generated. Nevertheless, the key quantity, debond resistance Γ, is measured and this can be used in device design. Debond resistance has been measured for a range of bimaterials for applications to thin films and fiber/matrix composites (Evans et al. 1990; Cannon et al. 1992).

In principle, test pieces of any geometry can be used to measure debond resistance. Several convenient geometries are sketched in Figure 12.6. It has been observed experimentally that debond resistance depends on the geometry of the test-piece. Specifically, debond resistance depends on the ratio of the sliding to normal loading parameterized by ψ:

$$\Gamma = \Gamma(\psi) \qquad (12.15)$$

Mode mixity ψ will be elaborated upon later. The trend of the curve is shown in Figure 12.6. The double cantilever beam is predominantly opening mode ($\psi \approx 0°$) and the measured debond resistance is low. The fiber pullout is shear dominant ($\psi \approx 70°$), giving a high debond resistance. The other two, four-point bend and microindentation, produce nearly equal amounts of opening and shear ($\psi \approx 45°$), representative of the conditions in thin-film delamination and fiber/matrix debonding. Microindentation is particularly convenient for small samples (Davis et al. 1991). Other geometries have also been used to measure debond resistance (Argon et al. 1989; Kim 1991; Liechti and Chai 1992; O'Dowd et al. 1992a; Thouless 1990; Wang and Suo 1990).

The dependence of Γ on loading phase can be understood on the basis of inelastic mechanisms. For example, the fiber pullout experiment is dominated by shearing while friction adds to the debond resistance. This mechanism has been examined quantitatively by Hutchinson and Evans (1989). In metal/ceramic interfaces, shear-dominated loading produce larger plastic zones which increase debond resistance (O'Dowd et al. 1992b).

12.2 Williams' Singularity

This section collects mathematical details that refine the concept of mode mixity. The two solids are linearly

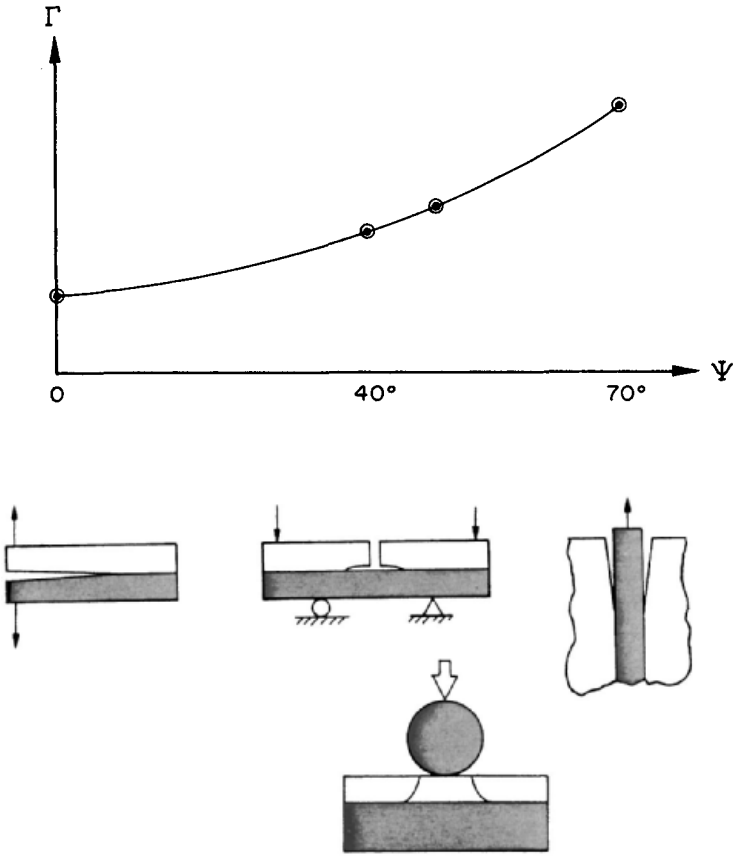

Figure 12.6. Convenient geometries to measure debond resistance.

elastic and isotropic; corresponding results for anisotropic elasticity have been reviewed elsewhere (Suo 1990). The inelastic region is taken to be small compared to all other relevant dimensions of the crack geometry, so that the crack front is a mathematical line, the interface is a mathematical plane, and the crack is semi-infinite. The crack faces are traction-free. This eigenvalue problem was solved by Williams (1959). The essential features of the solution, stress oscillation and crack face contact, are described below. The following interpretation is largely due to Rice (1988).

12.2.1 Slow Oscillation in Stress Field

The tractions at a distance r ahead of the crack tip, on the interface, are found to be

$$\sigma_{yy} + i\sigma_{yx} = \frac{Kr^{i\varepsilon}}{\sqrt{2\pi r}} \qquad (12.16)$$

In the above, x and y are Cartesian coordinates centered at the tip and $i = \sqrt{-1}$. The bimaterial constant ε is defined by

$$\varepsilon = \frac{1}{2\pi} \ln\left[\frac{(3-4\nu_1)/\mu_1 + 1/\mu_2}{(3-4\nu_2)/\mu_2 + 1/\mu_1}\right] \qquad (12.17)$$

Here ν is Poisson's ratio, μ the shear modulus, and subscripts 1 and 2 refer to material 1 and 2, respectively; the constant ε is bounded, $|\varepsilon| < (1/2\pi)ln3 \approx 0.175$.

The complex-valued stress intensity factor, K, cannot be determined by the eigenvalue problem, but can be determined by solving the full boundary-value problem for a given test-piece. The magnitude of K scales with the applied stress, and the phase angle of K represents the relative amount of shear to tension. It can be seen from (12.16) that K has the dimensions

$$K = [\text{stress}]\,[\text{length}]^{1/2 - i\varepsilon} \qquad (12.18)$$

Let $\hat{L}$ be an *arbitrary* length, and define $\hat{\psi}$ by

$$K = |K|\hat{L}^{-i\varepsilon}\exp(i\hat{\psi}) \qquad (12.19)$$

The magnitude, $|K|$, has the dimension stress $\times$ length$^{1/2}$, which is independent of the choice of $\hat{L}$, because $|\hat{L}^{i\varepsilon}| = 1$. Indeed, $|K|$ is related to $\mathcal{G}$ (Malyshev and Salganik 1965) by

$$\mathcal{G} = \frac{1}{4}\left(\frac{1-\nu_1}{\mu_1} + \frac{1-\nu_2}{\mu_2}\right)\frac{|K|^2}{\cosh^2 \pi\varepsilon} \qquad (12.20)$$

Consequently, $|K|$ and $\mathcal{G}$ are equivalent quantities characterizing the magnitude of the applied load.

Next examine the significance of $\hat{\psi}$. Combining Equations 12.16 and 12.19 yields

$$\sigma_{yy} + i\sigma_{yx} = \frac{|K|}{\sqrt{2\pi r}} \exp i[\hat{\psi} + \varepsilon \ln(r/\hat{L})] \qquad (12.21)$$

The identity, $(r/\hat{L})^{i\varepsilon} \equiv \exp[i\varepsilon \ln(r/\hat{L})]$, is used in the above. From Equation 12.21, the ratio of shear stress to tensile stress at a distance r ahead of the crack tip is given by

$$\sigma_{xy}/\sigma_{yy} = \tan[\hat{\psi} + \varepsilon \ln(r/\hat{L})] \qquad (12.22)$$

Observe that the traction ratio varies with position r, and that $\tan \hat{\psi}$ equals the ratio of the shear stress to the tensile stress at $r = \hat{L}$. This feature of interface cracks, caused by elastic mismatch, does not exist in mixed mode fracture in homogeneous materials. The result in Equation 12.22 is commonly referred to as the oscillatory singularity, and ε is referred to as the oscillation index. Contrary to a popular misconception, this oscillation is *not* rapid, because ε is small and because a logarithm is a slowly varying function. Thus, in specifying mode mixity, $\hat{L}$ need not be precisely defined, so long as it is broadly representative of the length scale of interest.

Up to this point, $\hat{L}$ has not been given any physical identity. Because Williams' elastic solution describes the stress state outside of the inelastic zone, it is sensible to specify $\hat{L}$ to be on the order of the inelastic zone size. For example, in discussing dislocation emission from an atomistically sharp crack tip, a natural choice of $\hat{L}$ is atomic spacing, so that $\hat{\psi}$ describes the stress state over several atomic spacing (Rice et al. 1990). For a metal/ceramic interface, where dislocation motion prevails over distances many times of the lattice constants, $\hat{L}$ should be chosen as the plastic zone size. Given two choices L and $\hat{L}$, the corresponding loading phases, ψ and $\hat{\psi}$, shift by

$$\psi - \hat{\psi} = \epsilon \ln(L/\hat{L}) \qquad (12.23)$$

Debond resistance Γ should depend on stress state surrounding the inelastic zone, which in turn is characterized by the local phase angle $\hat{\psi}$. Consequently, Equation 12.15 can be rewritten in a more rigorous form.

$$\Gamma = \Gamma(\hat{\psi}) \qquad (12.24)$$

Because the size of the inelastic zone depends on fracture mechanisms ranging from nanometers to centimeters, it is meaningless to employ a single $\hat{L}$ for all bimaterials. For interfaces with debond resistance sensitive to mode mixity, the value of $\hat{\psi}$, together with $\hat{L}$, must be reported together with the value of Γ. Moreover, a common $\hat{L}$ must be used in the definition of $\hat{\psi}$ when comparing toughness values at different mode mixities.

12.2.2 Small-Scale Contact

In a homogeneous material, crack faces come into contact under compression. By contrast, interface crack faces may come into contact regardless of loading condition. The size of the contact zone depends on the mode mixity. In composites, the fiber and the matrix may remain in contact because of the residual compression or asperities, sliding against friction during pullout. This provides an example of large-scale contact (Hutchinson and Jensen 1990). In many other technical problems, such as thin-film decohesion, contact zone is small compared to the overall dimension. This section provides a criterion for small-scale contact.

Williams elastic solution shows that the displacement jump at a distance r behind the crack tip is

$$\delta_y + i\delta_x = \left(\frac{1-\nu_1}{\mu_1} + \frac{1-\nu_2}{\mu_2}\right) \cdot \frac{Kr^{i\varepsilon}}{(1+2i\varepsilon)\cosh \pi\varepsilon}\sqrt{\frac{2r}{\pi}} \qquad (12.25)$$

From the above, the crack opening is

$$\delta_y = \delta \cos[\hat{\psi} + \varepsilon \ln(\hat{L}/r) - \tan^{-1}(2\varepsilon)] \qquad (12.26)$$

where $\delta = (\delta_x^2 + \delta_y^2)^{1/2}$ is the magnitude of the displacement jump. If $\hat{L}$ is interpreted as the process zone size, and if the crack is required to remain open, i.e., $\delta_y > 0$, within $\hat{L} < r < 100\hat{L}$, the mode mixity must be confined within

$$\begin{aligned} -\pi/2 + 2\varepsilon < \hat{\psi} < \pi/2 + 2.6\varepsilon \quad & \text{for } \varepsilon > 0 \\ -\pi/2 - 2.6\varepsilon < \hat{\psi} < \pi/2 + 2\varepsilon \quad & \text{for } \varepsilon < 0 \end{aligned} \qquad (12.27)$$

The number 100 is arbitrary, but the condition in Equation 12.27 is not sensitive to this number. When $\varepsilon = 0$, the above condition simply states that contact will not occur under tension, which is known for homogeneous materials.

12.2.3 Specimen Calibrations

For a given test piece, the complex stress intensity factor K can be solved by an elastic stress analysis. It has the generic form

$$K = YT\sqrt{L}L^{-i\varepsilon}\exp(i\psi) \qquad (12.28)$$

where T is a representative stress magnitude, and L a characteristic crack dimension. Y and ψ are dimensionless real numbers that depend on elastic constants, geometric parameters, and loading. Note that ψ is by definition the phase of $KL^{i\varepsilon}$. Solutions have been compiled by Hutchinson and Suo (1992).

As an example, consider a Griffith crack of length L on the interface between two materials (Figure 12.7). The complex stress intensity factor is

$$K = (1 + 2i\varepsilon)\sqrt{\pi L/2}L^{-i\varepsilon}T\exp(i\omega) \qquad (12.29)$$

where ω is the remote loading angle. Driving force $\mathcal{G}$ is obtained by substituting Equation 12.29 in Equation 12.20; the loading angle consistent with Equation 12.28 is $\psi = \omega + \tan^{-1}(2\varepsilon)$. The mode mixity at $r = \hat{L}$ is given by

$$\hat{\psi} = \omega + \tan^{-1}(2\varepsilon) + \varepsilon\ln(\hat{L}/L). \qquad (12.30)$$

For a numerical illustration, consider an alumina/glass interface ($\varepsilon = -0.05$). The crack size $L = 1$ mm, and the process zone size is of the order $\hat{L} = 1$ nm. Under remote tension, $\omega = 0°$, one finds $\hat{\psi} = 34°$, that is, a large shear component exists near the crack tip. Now change the crack size to $L = 1$ cm, and everything else being the same, the new phase angle becomes $\hat{\psi} = 40°$.

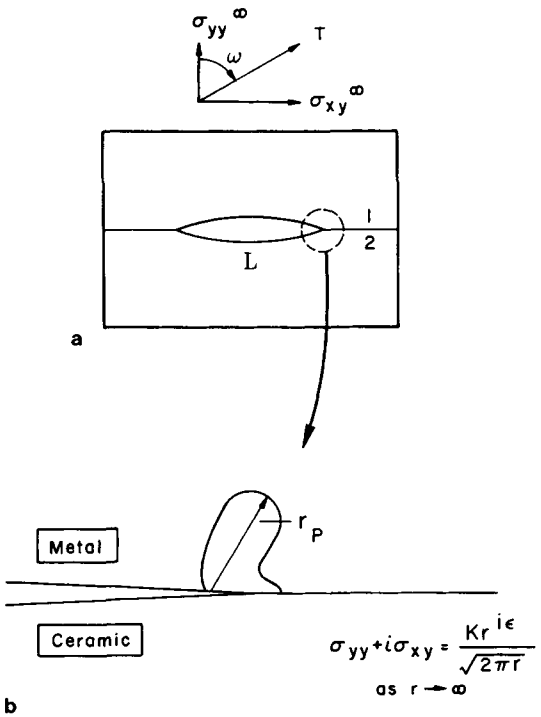

Figure 12.7. (a) A finite interface crack subjected to a remote tension T at angle ω; the plastic zone size is assumed to be small compared to the crack size. (b) A small-scaled yielding problem is posed.

12.3 Crack Tip Plasticity

Plastic flow around the tip of an interface crack has been analyzed by Shih and Asaro (1988), Shih et al. (1991), and Zywicz and Parks (1989, 1992). Plasticity aspects of interface cracks are reviewed by Shih (1991). Consider a stationary interface crack between two materials, at least one of which is plastically deformable (Figure 12.7). Small-scale yielding conditions prevail—that is, the plastic zone size r_p is much smaller than the characteristic specimen dimension (e.g., crack size L for a finite crack in an infinite body). Stress distribution over distances $r \gg r_p$ is approximately determined by elasticity, as if near-tip plasticity were nonexistent. In particular, the stress field in the annulus, $r_p \ll r \ll L$, is given by Williams' singular solution discussed in Section 12.2. The boundary value problem thus consists of two semi-infinite materials bonded over $x_1 > 0$, but unbonded over $x_1 < 0$; Williams' stress distribution is applied as boundary conditions as $r \to \infty$, with a complex stress intensity factor as follows:

$$K = |K|L^{-i\varepsilon}\exp(i\psi) \qquad (12.31)$$

Here L is the crack size, and ψ the load angle in the elasticity problem of finite crack. The elastic-plastic response is characterized by J_2 flow theory.

12.3.1 Plastic Zone Size

The problem contains two length scales, L and $(|K|/\sigma_Y)^2$, σ_Y being the lower yield stress of the two materials. Elementary considerations suggest that r_p scales with $(|K|/\sigma_Y)^2$, providing a natural length to define mode mixity. Define a dimensionless number by

$$\xi = \psi + \varepsilon\ln\left(\frac{|K|^2}{\sigma_Y^2 L}\right) \qquad (12.32)$$

According to the interpretation in Section 12.2.1, $\tan\xi$ broadly represents the traction ratio σ_{xy}/σ_{yy} near $r = (|K|/\sigma_Y)^2$, or just outside of the plastic zone.

The plastic zone size is given by

$$r_p = \mathcal{R}(|K|/\sigma_Y)^2 \qquad (12.33)$$

The dimensionless factor $\mathcal{R}$ depends weakly on material constants, but is sensitive to mode mixity, ranging from

0.15 to about 0.65 as $|\xi|$ increases from 0 to $\pi/2$. Furthermore, the shape of the plastic zone depends on the sign of ξ, which may lead to different debond resistance for loading with opposite shear directions. The above results are rigorously correct for deformation plasticity; numerical calculations have shown that they are quite accurate for flow theory.

12.3.2 *Stress Distribution Around a Blunted Crack Tip*

Next consider the stress distribution *within* the plastic zone. The region of interest is bounded by the plastic zone size r_p, and the crack tip opening displacement δ_t. The latter is given by

$$\delta_t = \mathfrak{D} J/\sigma_Y \qquad (12.34)$$

The prefactor, $\mathfrak{D}$, ranges from 0.5 to 0.7 for $|\xi| \leq \pi/6$ when the metal has low strain hardening ($N \leq 0.1$). The two lengths, r_p and δ_t, differ by a factor comparable to the yield strain.

The traction ratio, σ_{xy}/σ_{yy}, ahead of the blunted crack tip, within $\delta_t < r < r_p$, is shown in Figure 12.8. Note that $\tan \xi \approx \sigma_{xy}/\sigma_{yy}$ near $r = (|K|/\sigma_Y)^2$. For the opening mode $\xi \approx 0$, the traction ratio remains small over the range of distances shown. Under mixed mode loading $\xi \neq 0$, moderate variation in the traction ratio is observed. The trends displayed in Figure 12.8 are representative of metal/ceramic interfaces. Figure 12.9 shows the distribution of the hoop stress ahead of the crack tip. Focus on the curve for $\xi = 0$. The blunted crack tip relieves the constraint, leading to a low stress

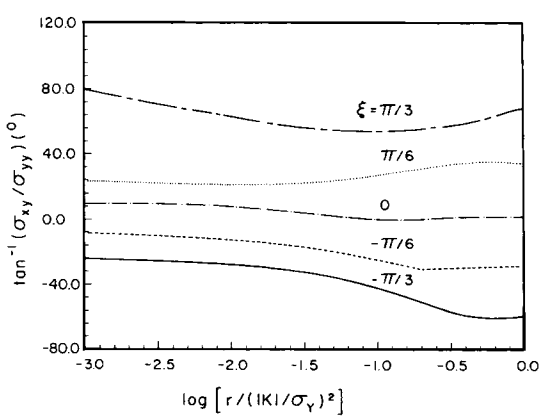

Figure 12.8. The ratio of shear over tension ahead of the crack tip, on the interface, in the range $\delta_t \leq r \leq r_p$. Metal/ceramic bimaterial; metal properties are $N = 0.1$, $\varepsilon_Y = 0.003$, and $\nu = 0.3$.

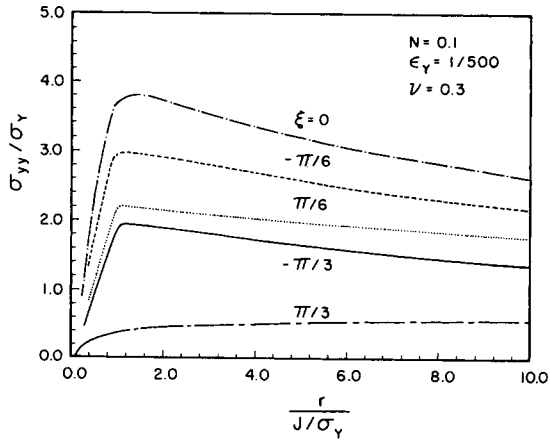

Figure 12.9. Tensile stress ahead of the crack tip, on the interface. Note that $\delta_t \sim J/\sigma_Y$. Metal/ceramic bimaterial; metal properties are $N = 0.1$, $\varepsilon_Y = 0.003$, and $\nu = 0.3$.

within $r < J/\sigma_Y$. The hoop stress reaches a maximum at distance $r \approx J/\sigma_Y$. The stiffer substrate provide additional constraint to plastic flow so that the stress for $\xi = 0$ is about 10% higher than the level for the corresponding homogeneous material (Shih et al. 1991). The constraint is partially relieved when the loading contains a large shear component.

In recent experiments with niobium diffusion bonded to alumina, O'Dowd et al. (1992b) found that debond resistance varies significantly with mode mixity; for example, $\Gamma(40°)/\Gamma(0°) \approx 10$. An attempt was made to correlate mixed mode debond resistance on the basis of a cleavage stress at a characteristic distance (for example, distance between triple point junctions in Al_2O_3), as an extension of the early work of Ritchie et al. (1973) on mode I fracture in mild steels.

The evolution of cyclic near-tip fields ahead of a stationary interface crack has been investigated by Woeltjen et al. (1992). Under monotonic loading to peak tensile load an essentially mode I near-tip field is observed over the major portion of the plastic zone, similar to the result in Figure 12.8 for $\xi = 0$. However, a mixed-mode field is generated near the tip upon removal of the tensile load. The development of strong shear tractions ahead of the interface crack tip has important implications for fatigue fracture mechanisms and fatigue life.

12.3.3 *Constrained Plasticity*

Reimanis et al. (1991) have carried out fracture experiments with gold foils that were diffusion bonded between sapphire plates. The foil thickness, h, is much smaller than the overall dimension of the specimen. The

plastic zone is comparable to (or even larger than) h, but the total inelastic zone size is small compared to specimen dimensions. Therefore, the remote load can be prescribed by a stress intensity factor. Upon loading, partial debond develops at a distance several times the foil thickness ahead of the crack tip. These micro-debonds do not connect with the crack tip. With furthur loading, new debonds nucleate at a even larger distance ahead of the crack tip, as shown in Figure 12.11(d). The intact metal ligaments bridge the crack, leading to a rapidly rising resistance curve (R—curve). Here we focus on the initiation of the micro-debond, the precursor to bridging.

The above phenomenon is an extreme form of large-scale yielding (relative to the foil thickness h), in which the metal foil is highly constrained by the sapphire plates. A finite element analysis by Varias et al. (1991, 1992) reveals that the hydrostatic stress in the metal foil increases steadily as the applied load increases; this is in contrast to the stress distribution ahead of an interface crack between two substrates that cannot elevate above three to four times the yield stress. The behavior of the mean stress in the metal foil is shown in Figure 12.10. Near the tip ($r/h \ll 1$), the stress distribution is not affected by the constraint of the foil thickness, so the mean stress is about three times the yield stress, similar to the distribution in Figure 12. 9. At a distance several times the foil thickness, the mean stress reaches the maximum, which increases with applied load; the location of the maxima shifts ahead as the load increases. These elevated stress maxima are responsible for micro-debonds.

12.4 Growing Cracks and Debond Resistance

Debonding rearranges the atoms that form the interface into two free surfaces, consuming the Griffith energy

$$\Gamma_G = \gamma_1 + \gamma_2 - \gamma_{int} \qquad (12.35)$$

Here γ_1 and γ_2 are the surface energies of material 1 and 2, respectively, and γ_{int} is the interface energy. The Griffith energy is small, since only a few layers of atoms participate in irreversible movements. To increase debond resistance, more atoms must be brought into the inelastic process, through mechanisms activated by stress lower than that required for atomic separation. For example, $\Gamma_G < 10$ J/m^2 for Al_2O_3, but even single crystal Al_2O_3 has fracture resistance exceeding 30 J/m^2. Some heat-dissipating, atomic-scale snapping processes might exist, involving atoms off the crack plane (K.-S. Kim, private communication). The fracture resistance of polycrystalline Al_2O_3 is further increased by grain-scale dissipating mechanisms such as pullout against friction (Vekinis et al. 1990).

Studies on crack growth resistance in metals were initiated by McClintock and Irwin (1965). They used small-scale yielding solutions for growing cracks in mode III, together with a growth criterion based on the attainment of a critical strain at a characteristic distance ahead of the tip. Later developments along this line were given by Drugan et al. (1982), and have been extended by Drugan (1991) and Ponte Castañeda and Mataga (1992) to cracks growing along bimaterial

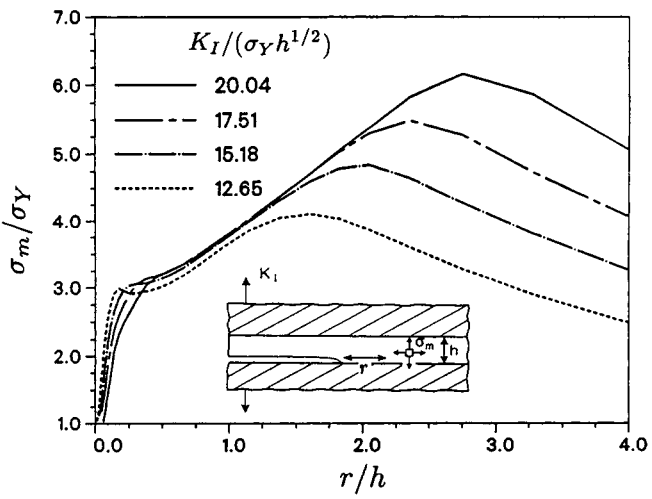

Figure 12.10. Inset: a metal foil bonded between two ceramic substrates, subjected to a remote Mode I stress intensity factor. The mean stress distribution ahead of the crack tip is plotted for several loading levels.

interfaces. Mechanism-based models to relate debond resistance to micromechanisms have been developed recently, and provide a focus for the subsequent presentation. We will limit our attention to predominantly opening mode of fracture.

12.4.1 Crack-Bridging

A solid will fall apart unless something holds it together. A far reaching, unifying idea, sufficiently rigorous for our purpose, is to represent "binding" by a relation between attractive stress, σ, and separation, δ. Such a relation is sketched in Figure 12.5, and is written as

$$\sigma/\sigma_B = \chi(\delta/\delta_B) \tag{12.36}$$

The dimensionless function χ describes the shape of the relation and the scale is set by σ_B and δ_B. The energy required to separate unit area of surfaces so bridged is

$$\Gamma_B = \sigma_B \delta_B \int_0^\infty \chi(\kappa) d\kappa \tag{12.37}$$

The dimensionless integral is of order unity. In practice, the shape function χ is difficult to determine precisely, but the quantities σ_B and δ_B are readily related to microstructural variables (Evans 1990). One can therefore estimate fracture resistance by

$$\Gamma_B \approx \sigma_B \delta_B \tag{12.38}$$

Sketched in Figure 12.11 are several bridging mechanisms, and Table 12.1 lists the representative values of σ_B, δ_B and Γ_B for these mechanisms. Atomic bond has high strength but small debond separation, resulting in a small fracture resistance. Ductile, crack-bridging ligaments give rise to a substantially higher fracture resistance; these ligaments are believed to operate in polycrystalline steels at lower shelf (Hoagland et al. 1972), and in a ceramic matrix containing metallic particles. In the latter, δ_B scales with the diameter of the particles. It remains unclear for polycrystalline steels whether δ_B is set by grain size or some other microstructural lengths. Holes can nucleate in ductile alloys around hard inclusions, or on metal/ceramic interface around pores or

Table 12.1. Illustrative Properties for Bridging Mechanisms

	σ_B(N/m^2)	δ_B(m)	$\Gamma_B \approx \sigma_B\delta_B$(J/m^2)
Atomic bond	10^{10}	10^{-10}	1
Ductile ligament	10^8	10^{-5}	10^3
Hole growth	10^9	10^{-4}	10^5
Metal foil	10^7	10^{-5}	10^2

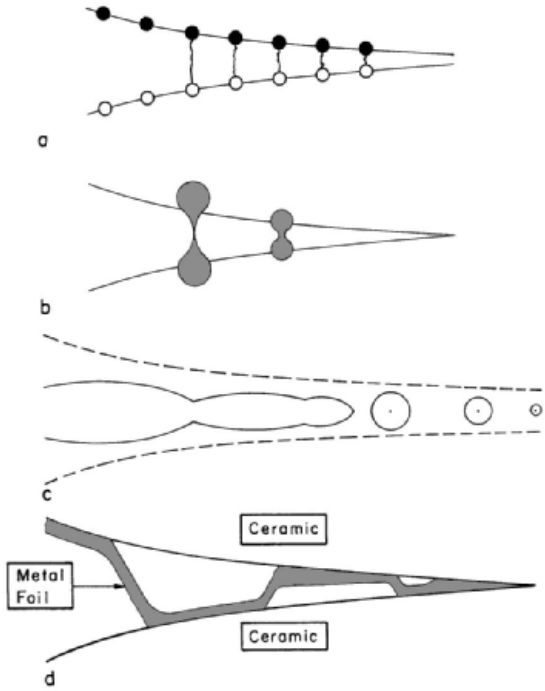

Figure 12.11. Crack-bridging mechanisms: (a) atomic adhesion, (b) ductile ligaments, (c) hole growth, and (d) alternating debonding.

triple-point junctions. Hole growth usually dissipates large amounts of energy. Thin metallic foils sandwiched between two ceramic substrates may debond along alternating interfaces, either because of periodic weak spots fabricated during bonding (Oh et al. 1988), or because of constrained plastic flow (Reimanis et al. 1991; Varias et al. 1991, 1992). More detailed review on crack-bridging concepts can be found elsewhere (Bao and Suo 1992; Suo et al. 1993).

12.4.2 Crack-Bridging and Background Plasticity

It is assumed in the previous section that inelastic deformation can be fully represented by a bridging law while the background material is elastic. In practice, several inelastic mechanisms can operate simultaneously. An interesting example involves a ceramic matrix containing both ductile and transforming particles. The ductile particles form bridges, while the transforming particles contribute to background dissipation. Bridging increases the height of the wake, transforming more particles and thereby dissipating more energy; transformation shields the bridging zone. Thus, the synergism (Amazigo and Budiansky 1988).

Consider the deformation history that a material at distance y off the interface experiences as the crack tip passes by. The energy density variation for the entire process is

$$W(y) = \int_0^{\varepsilon} \sigma_{ij} d\varepsilon_{ij} \qquad (12.39)$$

The integral is carried over the entire history, including the heat dissipation when the particle is in the active plastic zone, and the residual stress energy when the particle is in the wake. Let H_1 and H_2 be the depths of the inelastic layers in the two materials. The total energy expended in the background for the steady-state crack to move unit distance is

$$\Gamma_P = \int_{-H_2}^{H_1} W(y) dy \qquad (12.40)$$

The total fracture resistance, which includes Griffith energy, bridging energy, and stress work in the background, is given by

$$\Gamma = \Gamma_G + \Gamma_B + \Gamma_P \qquad (12.41)$$

Because Γ_P and Γ_B are typically much larger than Γ_G, it is sometimes assumed that Γ_G is an irrelevant parameter for fracture involving substantial plasticity. However, several authors have pointed out that if cleavage is the basic fracture mechanism, Γ_P or Γ_B must, in some way, depend on Γ_G — that is, the small quantity Γ_G serves as a "valve" for large dissipation Γ_B and Γ_P (Jokl et al. 1980). For example, in transformation-toughened ceramics, the matrix toughness sets the extent of the transformation zone and thereby Γ_P (McMeeking and Evans 1982; Budiansky et al. 1983).

A more familiar example is ductile fracture of alloys, where the near-tip mechanism of hole growth and coalescence serves as the valve for larger-scale plastic dissipation. This process has been analyzed by Needleman (1987, 1990), Varias et al. (1990), and Tvergaard and Hutchinson (1992). Consider a precut remotely loaded by a monotonically increasing $\mathcal{G}$. When $\mathcal{G} < \Gamma_B$, the bridging develops ahead of the crack tip, as does the plastic zone, while the crack remains stationary. The crack begins to grow or, rather, the bridges start to break when $\mathcal{G} = \Gamma_B$. In this sense, background plasticity does *not* provide any shielding prior to crack growth. This can be readily understood by the J-integral, and by the fact that plastic flow is proportional prior to crack growth. A reference length is defined by

$$R_B = \frac{1}{3\pi} \frac{\Gamma_B}{\sigma_Y \varepsilon_Y} \qquad (12.42)$$

This reference length scales with the extent of the plastic zone size when $\mathcal{G} = \Gamma_B$.

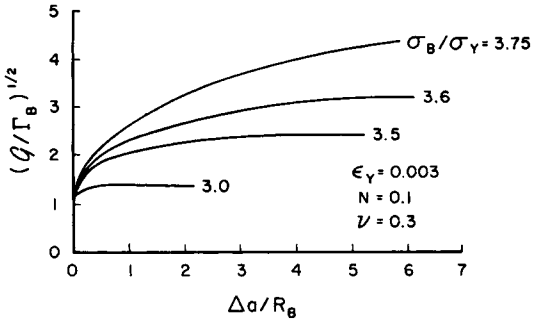

Figure 12.12. Fracture resistance curve resulting from background plasticity shielding. *(From Tvergaard and Hutchinson 1992.)*

As the crack grows, the bridging zone translates in the material: old bridges are broken in the wake, and new bridges are formed in the front. The background material also experiences elastic unloading and possibly reverse plastic loading. The complicated deformation shields the crack. The shielding ratio, $\mathcal{G}/\Gamma_B$, increases with the crack increment Δa, as shown in Fig 12.12. It is evident that the steady-state is established when the crack growth is greater than several times R_B. The steady-state fracture resistance, Γ_{SS}, depends on σ_B/σ_Y. The trend can be better seen in Figure 12.13. For a nonhardening material ($N = 0$), no contribution is derived from the background plasticity if $\sigma_B/\sigma_Y < 2$; conversely, the crack is "lock up," or has infinite fracture resistance when $\sigma_B/\sigma_Y \geq 3$. Similar trends are observed for strain-hardening materials.

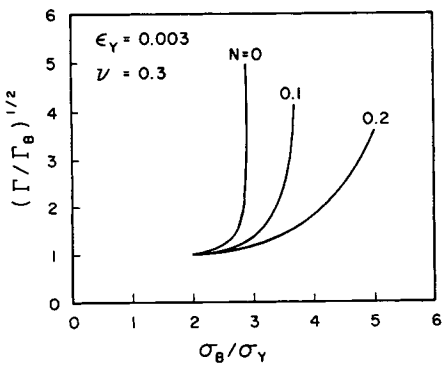

Figure 12.13. Steady-state shielding ratio as a function of bridging strength relative to yield strength. *(From Tvergaard and Hutchinson 1992.)*

12.4.3 *Brittle Debonding in the Presence of Plastic Flow*

It is known that a sharp, cleaving crack can propagate, slowly or dynamically, surrounded by substantial dislocation motion. For example, a sharp crack can grow slowly by cleavage along a gold/sapphire interface even though the gold deforms plastically; the measured fracture energy is much larger than Γ_G (Reimanis et al. 1991). Similar behavior is observed in copper/glass (Oh et al. 1987), copper/sapphire (Beltz and Wang 1992), niobium/alumina (O'Dowd et al. 1992b), and copper bicrystals contaminated by bismuth (Wang and Anderson 1991). This phenomenon cannot be explained by the models discussed in the previous sections. Atomic cohesive strength, σ_B, is known to be orders of magnitude higher than macroscopic yield strength, σ_Y. When σ_B/σ_Y exceeds about 4, crack-bridging models within the framework of continuum plasticity predict that the crack blunts, limiting the near-tip stress to several times σ_Y (Figure 12.9). Consequently, cleavage cannot proceed from the crack tip. Instead, one has to appeal to other fracture mechanisms, such as hole growth (Rice and Johnson 1970) and cleavage from a remote defect (Ritchie et al. 1973), both leading to rough fracture surfaces not observed in experiments cited in the previous paragraph.

Figure 12.14 conveys the essentials of a theory proposed by Suo et al. (1993). The fundamental process for plastic flow is discrete, consisting of at least two length scales: the Burgers vector $b \sim 10^{-10}$ m, and dislocation spacing $D \sim 10^{-6}$ m. On one scale, atoms exhibit individuality ultimately governed by quantum mechanics. On the other scale, dislocations interact through continuum elasticity. Continuum plasticity applies when stress variation over a multiple of D is small compared to the macroscopic yield strength. The discreteness becomes important for events occurring between lengths b and D.

The theory is based on a single premise: the crack front does not emit dislocations. This happens, for example, for cleavable materials such as steel and silicon below the ductile-brittle transition temperature, or contaminated grain boundaries, or interfaces subjected to environmental degradation, or interfaces with a few atomic layers of brittle reaction compounds. As illustrated in Figure 12.14, so long as dislocation spacing D is much larger than the lattice constant, the probability for a pre-existing dislocation to blunt a major portion of the crack front should be extremely small. Consequently, a crack that does not emit dislocation will remain nanoscopically sharp, advancing by atomic decohesion. Within the cell, essentially free of dislocations that surrounds the crack front, the crystal is linearly

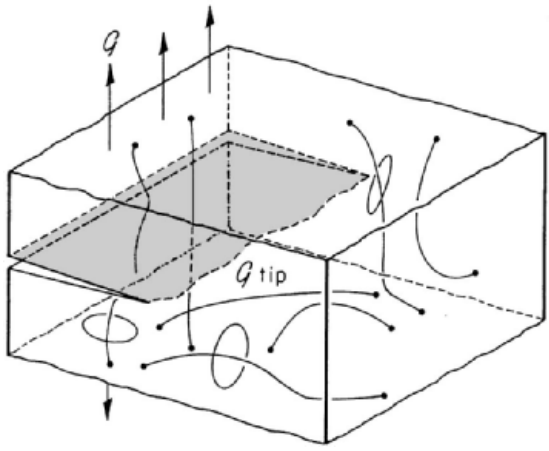

Figure 12.14. A decohesion front in a network of pre-existing dislocations. The diameter of the decohesion core is about 1 nm; the average dislocation spacing is more than 100 nm.

elastic down to a nanometer. Near the crack tip, nonlinearity arises from partial atomic separation and nanoscopic shear bands. The size of the elastic cell, represented by D, is several orders of magnitude larger than the nonlinear zone size. Consequently, information regarding the nanoscopic nonlinearity is transmitted—to an observer outside the elastic cell—through a single quantity: the Griffith energy Γ_G. The elastic cell provides a medium through which the stress decays rapidly, matching the high atomic debond stress on one side, and the low macroscopic yield stress on the other. For example, with $b = 10^{-10}$m and $D = 10^{-6}$m, the stress decays approximately by a factor $\sqrt{D/b} = 100$ over a distance of 1 μm. The dislocation motion at the characteristic distance D away from the crack tip dissipates plastic energy, Γ_P, which is typically much larger than Γ_G. In summary, atoms around a crack front can be divided into three regions: nanoscopic decohesion zone, microscopic elastic cell, and macroscopic dislocation dissipative background.

The elastic cell is a nanomechanics concept with imprecise, if any, continuum description. The concept can be approximately understood in terms of spatially varying yield strengths. Sketched in Figure 12.15 is yield strength varying with the distance from a representative atom at the crack tip. The theoretical shear strength is approached near the crack tip; the strength decays to the macroscopic yield strength in the background. The shape of the decay function has not been investigated; dislocation cell models may provide some

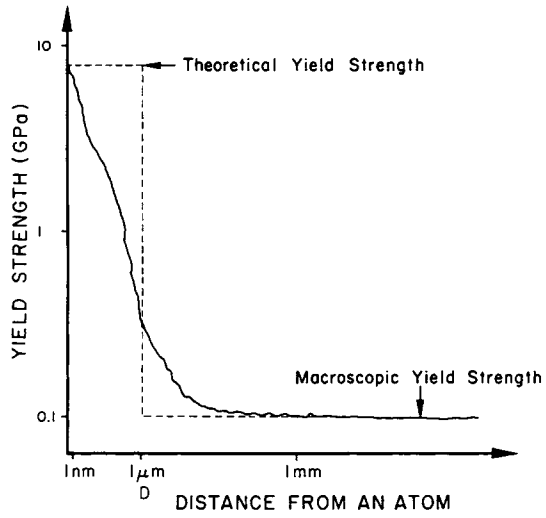

Figure 12.15. Yield strength as a function of the distance from an atom at the center of an elastic cell.

insight (Lubarda et al. 1993; Kubin et al. 1992). Nevertheless, the decay function *must* have a characteristic length comparable to the dislocation spacing D.

Consider a cleavable, rate-independent material with Griffith energy Γ_G, yield strength σ_Y and yield strain $\epsilon_Y = \sigma_Y/E$, E being Young's Modulus. The crack tip energy release rate, $\mathcal{G}_{tip}$, is shielded by background dislocation motion from the remotely applied energy release rate, $\mathcal{G}$. Dimensional analysis dictates that

$$\mathcal{G}/\mathcal{G}_{tip} = g(D\epsilon_Y\sigma_Y/\mathcal{G}_{tip}) \qquad (12.43)$$

The shielding ratio g also depends on crack increment and material constants such as ϵ_Y, Poisson's ratio ν and in particular, the shape of the decay function in Figure 12.15. For properties representative of metals (e.g. $D \sim 1\ \mu m$, $\epsilon_Y \sim 10^{-3}$, $\sigma_Y \sim 10^8\ N/m^2$, $\Gamma_G \sim 1\ J/m^2$), the parameter $D\ \epsilon_Y\sigma_Y/\Gamma_G$ ranges from 10^{-2} to 10. The parameter can be understood in several ways; e.g., all else being fixed, an increase in elastic cell size D reduces the total energy dissipation. Under steady-state growth, $\mathcal{G}_{tip} = \Gamma_G$ and $\mathcal{G}$ equals the measured fracture energy Γ. The plastic dissipation Γ_P is given by $\Gamma = \Gamma_P + \Gamma_G$.

In the present theory, it is assumed that no low strength, long range bridges, such as tearing caused by cleavage plane reorientation between neighboring grains, operate in the crack wake. These bridges are responsible for the large "cleavage energy" reported for polycrystalline steels. When operating, the bridges may serve as a bigger valve than atomic decohesion. If this is the case, a bridging law may be used in the present model. Indeed, when $\sigma_B/\sigma_Y < 4$, the present model should reduce to a regular bridging model without an elastic cell.

Further simplifications are needed to make quantitative predictions (Figure 12.16). The decohesion zone is small compared to D so that the square root singular elasticity solution prevails in $b \ll r \ll D$. Detailed atomistic description of decohesion is unnecessary except for a prescription of a cleavage energy Γ_G. The shape of the elastic cell is unimportant because the plastic zone height is typically much larger than D; we use a strip to represent the elastic cell. A disc translating with the crack tip can be another convenient choice, but the difference is expected to be minor in so far as $\mathcal{G}/\mathcal{G}_{tip}$ is concerned. The background dislocation motion is represented by continuum plasticity. A refinement, if needed, may include individual dislocations or a dislocation network in the transition region between the elastic cell and the continuum plastic flow.

The crack starts to grow when $\mathcal{G} \geq \Gamma_G$; more load is required to maintain the growth, leading to a resistance curve. The plastic zone also increases as the crack grows, attaining a steady-state height H. The energy release rate reaches a steady-state value Γ_{SS}. The model geometry is analyzed in the steady-state using finite elements. Figure 12.17 shows that the shielding ratio increases rapidly as D or σ_Y decrease. The influence of strain hardening exponent, N, can also be seen. For nonhardening metals, the plastic dissipation completely shields the crack tip at a finite $D\ \epsilon_Y\sigma_Y/\mathcal{G}_{tip}$. In practice, D may be used as a fitting parameter to correlate experimental data. For example, a metal with $\sigma_Y = 10^8\ N/m^2$, $\epsilon_Y = 3.3 \times 10^{-3}$ and $\Gamma_G = 2\ J/m^2$ gives $\Gamma_G/\sigma_Y\epsilon_Y = 6\ \mu m$. If the measured fracture energy $\Gamma_{SS} = 20\ J/m^2$, one finds from Figure 12.17 that $D \approx 0.1\ \mu m$.

In an experiment with a single crystal of copper diffusion bonded to a sapphire disc (Beltz and Wang

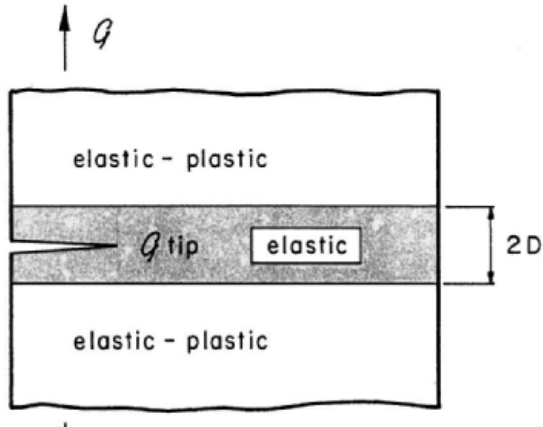

Figure 12.16. A model system with a step-function decay in yield strength.

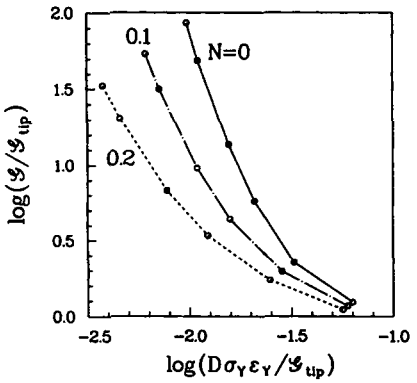

Figure 12.17. A fracture resistance curve: the fracture energy increases as the crack grows. Computed shielding ratio as a function of various parameters: N—hardening exponent, D—elastic cell size.

1992), interface debonding was driven in two crystallographic directions at slightly different energy release rates. The phenomenon was interpreted according to the Rice-Thomson model (1974): dislocations emit from the crack tip in one direction but not from the other. An alternative interpretation appears to be possible on the basis of the present theory: both crack tips do not emit dislocations and the different debond energies result from the different extent of background dislocation motion. Indeed, the micrographs show much denser slip lines in one case than they do in the other. Experiments at higher magnifications are needed to ascertain which of the two interpretations is appropriate for the copper/sapphire system. Calculations within the framework of the present theory, taking into account single crystal plasticity, are in progress to facilitate a direct comparison with such experiments.

Obviously, the competition between atomic decohesion and dislocation emission (Rice et al., 1992) cannot be addressed by the present theory. Instead, the consequences of the premise that dislocations do not emit from the crack front can be explored. Included in Suo et al. (1993) are slow cleavage cracking, stress-assisted corrosion, fast-running crack, fatigue cracking, constraint effects, and mixed mode fracture along metal/ceramic interfaces.

Acknowledgements

The work of Z.S. was supported by an NSF Young Investigator Award, by DARPA/URI Contract N00014-86-K-0753, and by a Visiting Associate Professor appointment at Brown University funded by NRC/ONR Grant N00014-90-J1380. The work of C.F.S. was supported by NRC/ONR Grant N00014-90-J13800, and by the Materials Research Group funded by NSF through Grant DMR-9002994.

References

Amazigo, J.C., and B. Budiansky. 1988. *J. Mech. Phys. Solids.* 36:581–595.

Aveston, J., Cooper, G.A., and A. Kelly. 1971. *In:* The Properties of Fiber Composites. Conference Proceedings, National Physical Laboratory (Guildford UK). 15–24, Teddington, UK: IPC Science and Technology Press, Ltd.

Argon, A.S., Gupta, V., Landis, H.S., and J.A. Cornie. 1989. *J. Mater. Sci.* 24:1406–1412.

Ashby, M.F., Rühle, M. (eds.). 1992. Proceedings of International Symposium on Metal/Ceramic Interfaces. To be published in *Acta Metall. Mater.*

Bao, G., and Z. Suo. 1992. *Appl. Mech. Rev.* In Press.

Beltz, G.E., and J.-S. Wang. 1992. *Acta Metall. Mater.* 40:1675–1683.

Budiansky, B., Hutchinson, J.W., and J.C. Lambropoulos. 1983. *Int. J. Solids Struct.* 19:337–355.

Cannon, R.M., Dalgleish, B.J., Dauskardt, R.H. et al. 1992. *In:* Fatigue of Advanced Materials (R.O. Ritchie, R.H. Dauskardt, and B.N. Cox, eds.) Edgbaston, UK: MCEP Publishing Ltd.,

Cao, H.C., and Evans, A.G. 1989. *Mech. Mater.* 7:295–305.

Cottrell, A.H. 1963. *In:* Tewksbury Symposium on Fracture. 1–27, Melbourne: University of Melbourne.

Davis, J.B., Cao, H.C., Bao, G., and A.G. Evans. 1991. *Acta Metall. Mater.* 39:1019–1024.

Drugan, W.J. 1991. *J. Appl. Mech.* 58:111–119.

Drugan, W.J., Rice, J.R., and T.-L. Sham. 1982. *J. Mech. Phys. Solids.* 30:447–473.

England, A.H., 1965. *J. Appl. Mech.* 32:400–402.

Erdogan, F. 1965. *J. Appl. Mech.* 32:403–410.

Evans, A.G. 1990. *J. Am. Ceram. Soc.* 73:187–206.

Evans, A.G., Drory, M.D., and M.S. Hu. 1988. *J. Mater. Res.* 3:1043–1049.

Evans, A. G., and J.W. Hutchinson. 1989. *Acta Metall. Mater.* 37:909–916.

Evans, A.G., Rühle, M., Dalgleish, B.J., and P.G. Charalambides. 1990. *Mater. Sci. Eng.* A126:53–64.

Farris, R.J., and C.L. Bauer. 1988. *J. Adhesion.* 26:293–300.

Griffith, A.A. 1921. *Phil. Trans. Roy. Soc. Lond.* A221:163–197.

Hoagland, R.G., Rosenfield, A.R., and G.T. Hahn. 1972. *Metall. Trans.* 3:123–136.

Hutchinson, J.W. 1979. Nonlinear Fracture Mechanics. Department of Solid Mechanics, Technical University of Denmark.

Hutchinson, J.W., and H.M. Jensen. 1990. *Mech. Mater.* 9:139–163.

Hutchinson, J.W., and Z. Suo. 1992. *Adv. Appl. Mech.* 29:63–191.

Irwin, G.R. 1960. *In:* Structural Mechanics. (J.N. Goodier and N.J. Hoff, eds.), 557–591, Oxford: Pergamon Press.

Jokl, M.L., Vitek, V., and C.J. McMahon, Jr. 1980. *Acta Metall.* 28:1479–1488.

Kanninen, M.F., and C.H. Popelar. 1985. Advanced Fracture Mechanics. Oxford: Oxford University Press.

Kim, K.-S. 1991. *Mat Res Soc Symp Proc.* 203:3–14.

Kubin, L.P., Canova, G., Condat, M. et al. 1992. *In:* Nonlinear Phenomena in Materials Science II (G. Martin and L. P. Kubin, eds.). In press.

Liechti, K.M., and Y.-S. Chai. 1992. *J. Appl. Mech.* 59:295–304.

Lubarda, V.A., Blume J.A., and A. Needleman. 1992. *Acta Metall. Mater.* 41:625–642.

Malyshev, B.M., and R.L. Salganik. 1965. *Int. J. Fract. Mech.* 5:114–128.

McClintock, F.A., and G.R. Irwin. 1965. ASTM-STP 381, 84–113, Philadelphia: ASTM.

McMeeking, R.M., and A.G. Evans. 1982. *J. Am. Ceram. Soc.* 65:242–246.

Moran, B., and C.F. Shih. 1987. *Eng. Fract. Mech.* 27:615–642.

Needleman, A. 1987. *J. Appl. Mech.* 54:525–531.

Needleman, A. 1990. *J. Mech. Phys. Solids.* 38:289–324.

O'Dowd, N.P., Shih, C.F., and M.G. Stout. 1992a. *Int. J. Solids Struct.* 29:571–589.

O'Dowd, N.P., Stout M.G., and C.F. Shih. 1992b. *Phil. Mag.* 66A:1037–1064.

Oh, T.S., Cannon, R.M., and R.O. Ritchie. 1987. *J. Am. Ceram. Soc.* 70:C352–C355.

Oh, T.S., Cannon, R.M., and R.O. Ritchie. 1988. *Acta Metall.* 36:2083–2093.

Ponte Castañeda, P., and P.A. Mataga. 1992. Submitted for publication.

Reimanis, I.E., Dalgleish, B.J., and A.G. Evans. 1991. *Acta Metall. Mater.* 39:3133–3141.

Rice, J.R. 1968. *J. Appl. Mech.* 35:379–386.

Rice, J.R. 1988. *J. Appl. Mech.* 55:98–103.

Rice, J.R., Beltz, G.E., and Y. Sun. 1992. *In:* Topics in Fracture and Fatigue. (A.S. Argon, ed.), 1–58, Berlin: Springer-Verlag.

Rice J.R., and M.A. Johnson. 1970. *In:* Inelastic Behavior of Solids. (M.F. Kanninen, W.F. Adler, A.R. Rosenfield, and R.I. Jaffee, eds.), 641–672, New York: McGraw-Hill.

Rice, J.R., and G.C. Sih. 1965. *J. Appl. Mech.* 32:418–423.

Rice, J.R., Suo, Z., and J.S. Wang. 1990. *In:* Metal-Ceramic Interfaces, Acta-Scripta Metallurgica Proceedings Series (M. Rühle, A.G. Evans, M.F. Ashby, and J.P. Hirth, eds.), Vol. 4, 269–294, Oxford: Pergamon Press.

Rice, J.R., and R.M. Thomson. 1974. *Phil. Mag.* 29:73–97.

Rice, J.R., and J.S. Wang. 1989. *Mater. Sci. Eng.* A107:23–40.

Ritchie, R.O., Knott, J.F., and J.R. Rice. 1973. *J. Mech. Phys. Solids.* 21:395–410.

Rivlin, R.S., and A.G. Thomas. 1953. *J. Polym. Sci.* 10:291–318.

Rühle, M., Evans, A.G., Ashby, M.F., and J.P. Hirth (eds.) 1990. Metal-Ceramic Interfaces, Acta-Scripta Metallurgica Proceedings Series, Vol. 4. Oxford: Pergamon Press.

Shih, C.F. 1991. *Mater. Sci. Eng.* A143:77–90.

Shih, C.F., and R.J. Asaro. 1988. *J. Appl. Mech.* 55:299–316.

Shih, C.F., Asaro, R.J., and N.P. O'Dowd. 1991. *J. Appl. Mech.* 58:450–463.

Stump, D.M., and B. Budiansky. 1989. *Acta Metall. Mater.* 37:3297–3304.

Suo, Z. 1990. *Proc. R. Soc. Lond.* A427:331–358.

Suo, Z., Shih, C.F., and A.G. Varias. 1993. A Theory for Cleavage Cracking in the Presence of Plastic Flow. *Acta Metall. Mater.* 41:1551–1557.

Suresh, S., and A. Needleman, eds. 1989. Interfacial Phenomena in Composites: Processing, Characterization and Mechanical Properties. London: Elsevier Applied Science.

Thouless, M.D. 1990. *Acta Metall.* 38:1135–1140.

Tvergaard, V., and J.W. Hutchinson. 1992. *J. Mech. Phys. Solids.* 40:1377–1397.

Varias, A.G., O'Dowd, N.P., Asaro, R.J., and C.F. Shih. 1990. *Mater. Sci. Eng.* A126:65–93.

Varias, A.G., Suo, Z., and C.F. Shih. 1991. *J. Mech. Phys. Solids.* 39:963–986.

Varias, A.G., Suo, Z., and C.F. Shih. 1992. *J. Mech. Phys. Solids.* 40:485–509.

Vekinis, G., Ashby, M.F., and P.W.R. Beaumont. 1990. *Acta Metall. Mater.* 38:1151–1162.

Wang, J.S., and P.M. Anderson. 1991. *Acta Metall. Mater.* 39:779–792.

Wang, J.S., and Suo, Z. 1990. *Acta. Metall. Mater.* 38:1279–1290.

Williams, M.L. 1959. *Bull. Seismol. Soc. Am.* 49:199–204.

Woeltjen, C., Shih, C.F., and S. Suresh. 1993. "Near-Tip Fields for Fatigue Cracks along Metal–Metal and Metal–Ceramic Interfaces." *Acta Metall. Mater.* 41:2317–2335.

Zywicz, E., and D.M. Parks. 1989. *J. Appl. Mech.* 56:577–584.

Zywicz, E., and D.M. Parks. 1992. *J. Mech. Phys. Solids.* 40:511–536.